PCCP

ROYAL SOCIETY OF CHEMISTRY

PAPER

View Article Online
View Journal | View Issue

Cite this: *Phys. Chem. Chem. Phys.*, 2022, **24**, 15068

Torsional fracture of carbon nanotube bundles: a reactive molecular dynamics study†

Marcelo Lopes Pereira Júnior, [a] Tainá de Sousa Oliveira,[b] Fábio Ferreira Monteiro, [b] Wiliam Ferreira da Cunha,[b] Pedro Henrique de Oliveira Neto [b] and Luiz Antônio Ribeiro Júnior *[b]

Received 5th April 2022,
Accepted 27th May 2022

DOI: 10.1039/d2cp01589g

rsc.li/pccp

Carbon nanotubes individually show excellent mechanical properties, being one of the strongest known materials. However, when assembled into bundles, their strength reduces dramatically. This still limits the understanding of their scalability. Here, we perform reactive molecular dynamics simulations to study the mechanical resilience and fracture patterns of carbon nanotube bundles (CNTBs) under torsional strain. The results revealed that the fracture patterns of CNTBs are diameter-dependent. The larger the tube diameter, the higher the plasticity degree of the bundle sample when subjected to torsional loading. Tube chirality can also play a role in distinguishing between the CNTBs during the torsion process. Armchair-based CNTBs have higher accumulated energies and, consequently, higher critical angles for the bundle fracture when contrasted with CNTBs composed of zigzag or chiral nanotubes. Remarkably, the CNTB torsional fracture can yield nanodiamondoids.

1 Introduction

Carbon nanotubes (CNTs) are nanomaterials with sp^2 carbon-carbon bonds arranged in a tubular structure formed of rolled-up graphene sheets.[1,2] CNTs exhibit remarkable properties, some of which derive from graphene itself,[3] such as its lightweight,[4] good transparency,[5] high mechanical strength,[6] and high conductivity.[7] Their applications in nanotechnology include, among several others, bulletproof vests,[8,9] resonators,[10] gigahertz oscillators,[11] sensors,[12,13] energy storage,[14,15] and transistors.[16,17] In many cases, CNTs are self-organized into crystalline bundles, which are vertically aligned next to one another.[18] CNTs individually show excellent mechanical properties, being one of the strongest known materials.[19] However, when assembled into bundles, their strength reduces dramatically.[20]

Recently, several experimental[21–26] and theoretical[18,27–38] studies have investigated the mechanical properties of carbon nanotube bundles (CNTBs) in the form of long yarns,[23,34] nanofibers,[28] nanoropes,[27,32] and crystals.[18,36] Usually, torsional and tensile loadings are applied to analyze the behavior of these materials upon stress. Baughman and coworkers experimentally designed CNT yarns as electrolyte-free muscles that provide fast, high-force, large-stroke torsional, and tensile actuation.[23] Molecular dynamics simulations were used to understand the torsional buckling of pristine and irradiated CNTs.[29,31,33,35–37] As a general trend, these studies observed that in pristine CNTs, van der Waals (vdW) interactions are considered a crucial parameter in defining the mechanical and structural properties of the CNTBs upon torsional loading. During the twisting process, the increase in the interaction area by twisting the CNTB enhances the inter-tube interactions up to a critical angle. When this threshold is exceeded, the large cross-section deformations decrease the inter-tube shear strength. This process is responsible for the CNTB unpacking, which dramatically diminishes its torsional stiffness.[35] On the other hand, irradiation-induced inter-tube defects can significantly increase the critical buckling torque and critical buckling angle while slightly increasing the torsional stiffness.[37] Albeit some relevant studies have investigated the mechanical properties of single CNTs and CNTBs upon torsional loading, their fracture patterns, and possible products yielded in this process remain not described. In this sense, our investigation can shed light on the mechanical properties of CTBs under extreme conditions, contributing to their better understanding.

Herein, we carried out fully-atomistic reactive molecular dynamics (MD) simulations to study the torsional fracture of CNTBs and their underlying mechanical properties. We considered CNTBs of different diameters and chiralities. In this sense, we were able to map different products yielded after the CNTB fracture. Our findings showed that the CNTB fracture patterns are diameter-dependent. Tube chirality can also play a

[a] *Department of Electrical Engineering, Faculty of Technology, University of Brasília, Brasília, Brazil*
[b] *Institute of Physics, University of Brasília, Brasília, Brazil. E-mail: ribeirojr@unb.br*

† Electronic supplementary information (ESI) available. See DOI: https://doi.org/10.1039/d2cp01589g

role in distinguishing between the CNTBs during the torsion process. Remarkably, the CNTB torsional fracture can yield nanodiamondoids.

2 Methodology

To study the fracture patterns of CNTBs when subjected to torsional loading, we used fully-atomistic reactive MD simulations as implemented in the Large-scale Atomic/Molecular Massively Parallel Simulator (LAMMPS)[39] software. The adaptive-interatomic reactive bond-order (AIREBO) potential[40] was adopted. This reactive potential allows the formation and dissociation of chemical bonds. These features are crucial for describing the mechanical properties and fracture patterns of nanostructures under extreme conditions. We used CNTs of different chiralities and diameters to compose the bundles. The CNTBs are formed by seven CNTs, arranged in a triangular lattice, *i.e.*, the geometric center of six tubes is localized at the vertices of a regular hexagon, and the geometric center of one of these tubes coincides with the center of the hexagon. Table 1 summarizes the structural information on the diameters of CNTs and CNTBs and the number of atoms.

The effects of chirality and diameter on the twisting process of CNTBs were investigated using six different cases (see Table 1), *i.e.*, two different diameters for each chirality. The CNTs that are used to form the CNTBs are identical. The atomic structure of a carbon nanotube can be defined by the chiral indexes, (n,m), that specify its perimeter vector (chiral vector), with which the diameter and helicity are also determined.[41] In this sense, (n,n), $(n,0)$, and $(n,m < n)$ refer to nanotubes with armchair, zigzag, and chiral arrangements, respectively. The inter-tube distance is d = 2 Å. Fig. 1(a) shows the longitudinal view of the CNTB, where its length in all cases is 20 nm. Note that the edges were fixed (about 10 Å, highlighted in gray in Fig. 1(a)). In the twisting process, one of the edges remains fixed, while the other edge rotates around the central axis of the structure (in the longitudinal direction) for a given θ angle. Fig. 1(b) shows the front view of the CNTBs. Fig. 1(c)–(e) present the armchair, chiral and zigzag chiralities, respectively, for the largest diameter cases studied here. Fig. 1(f) shows the parameters involved in the CNTB twisting process: the CNT diameter (D), the inter-tube distances (d), and the twisting direction defined by θ angle. In the twisting process, five complete cycles were performed. In this sense, the maximum value of θ is 1800°. Table 1 summarizes the structural information on the CNTs and CNTBs diameters and number of atoms. The CNTBs were designed using Nanotube Modeler software.[42] They were prepared for simulation using Visual Molecular Dynamics (VMD) software.[43] VMD was also used to obtain the MD snapshots and videos.

The reactive potential used in the simulations was presented in the literature by Stuart *et al.*[40] This potential describes interactions between C–C, C–H, and H–H atoms. The simulation occurs at room temperature, with a time-step of 2×10^{-4} ps, and a rotation period of 300 ps (0.021 rad ps^{-1}), over a total of five turns, which are enough to realize the complete rupture of the CNTBs. The equations of motion are integrated from the Velocity-Verlet algorithm,[44] while the pressure is controlled using the Nosé-Hoover thermostat.[45,46] Previous to torsion, the structure is subjected to a constant-temperature equilibration, for 50 ps, with a canonical *NVT* ensemble to eliminate any residual stress before the CNTB twisting.

Table 1 Structural information on the CNTs and CNTBs investigated here. The CNTB diameter is given by $3D + 2d$, where D is the CNT diameter, and d is the inter-tube distance. The number of atoms in each nanotube can be obtained by dividing the number of atoms in the CNTB by seven. The atomic structure of a carbon nanotube can be defined by the chiral indexes, (n,m), that specify its perimeter vector (chiral vector), with which the diameter and helicity are also determined. In this sense, (n,n), $(n,0)$, and $(n,m < n)$ refer to nanotubes with armchair, zigzag, and chiral arrangements, respectively

	CNT	CNTB	
CNT(n,m)	Diameter Å	Diameter Å	Num. atoms
(3,3)	4.07	16.20	6846
(5,0)	3.91	15.74	6580
(4,2)	4.14	16.44	6958
(14,14)	18.98	61.00	31 948
(25,0)	19.57	62.76	32 900
(18,9)	18.64	59.96	31 311

3 Results

We show in Fig. 2 the MD snapshots for the twisting process of a CNTB formed with CNTs(3,3) at 300 K, from now on referred to as CNTB@CNT(3,3), as the representative case for systems with smaller tube diameters. The morphological deformations of CNTB@CNT(3,3) under torsional loading are analyzed until their complete fracture. In this way, Fig. 2(a)–(f) illustrate the MD snapshots for the CNTB@CNT(3,3) subjected to twisting angles of 0°, 360°, 720°, 1005°, 1260°, and 1440°, respectively. Importantly, the ESI,† presents videos of the MD simulations for the morphological deformations under torsional loading of all CNTBs studied here. In these videos, as a first result, one can conclude that the CNTBs fracture processes occur in the same fashion for tubes with a similar diameter (D).

Fig. 2(a) presents the CNTB@CNT(3,3) arrangement after its equilibration, *i.e.*, the initial structure for the twisting process. Temperature effects and vdW interactions play the role of displacing one tube concerning the other, slightly misaligning the whole structure. In Fig. 2(b) and (c), one can note that the application of torsional loading leads to twisting of each external CNT (*i.e.*, the six nanotubes localized at the vertices of a regular hexagon that forms the bundle) around the tube in the center of the bundle. The identical torsion mechanism of the external CNTs results in the twisting of the bundle around its longitudinal axis as a whole structure. Further increase in the torsional loading results in the failure of the CNTB@CNT(3,3), which is triggered by the fracture of three CNTs at θ = 1005°, as illustrated in Fig. 2(d). These tubes are

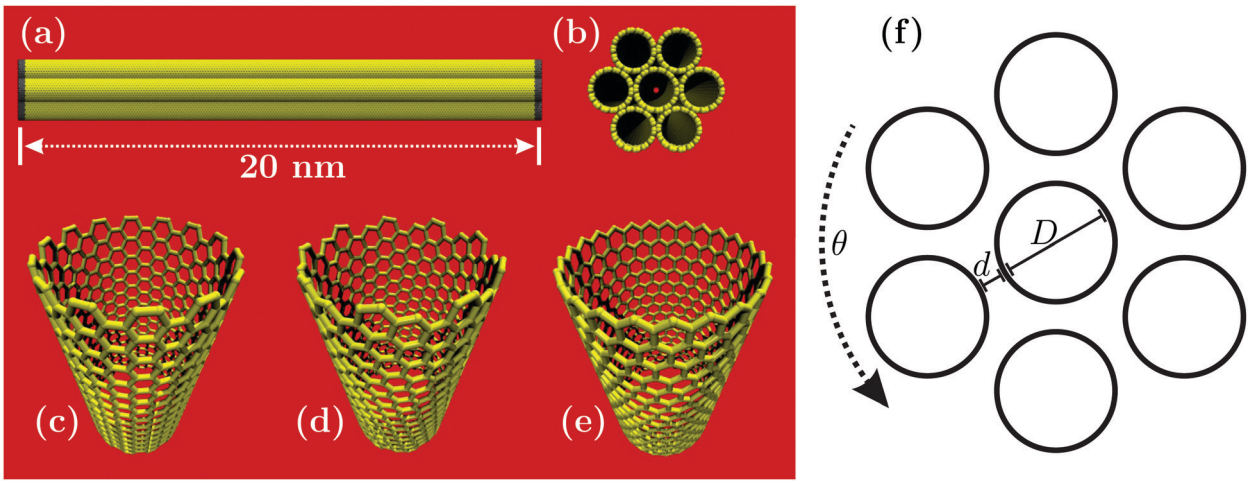

Fig. 1 Initial configuration of the CNTBs investigated in this work. Panel (a) shows the longitudinal view of the structure. In all cases, the CNTB length is approximately 20 nm. Panel (b) shows the front view of the CNTB arrangement. Panels (c)–(e) illustrate the armchair, chiral, and zigzag CNTs, respectively. These are the different chiralities used in the bundle assembly. Panel (f) shows the parameters involved in the CNTB twisting process: the CNT diameter (D), the inter-tube distances (d), and the twisting direction defined by θ angle.

unwrapped from the bundle structure since the temperature effects overcome the inter-tube shear strength, which is mediated by weak vdW interactions. With 3.5 cycles (Fig. 2(e)), large cross-section deformations take place, and the tubes remaining in the bundle collapse into a single structure that forms a defective region, highlighted in the yellow square. Interestingly, this defective region is constantly reconfigured (through several formation and braking of new bonds) during the twisting process without its total rupture, as depicted in Fig. 2(f). Later, we discuss the final product formed in this defective region. The ESI,† presents a discussion on the shear stress distribution (von-Mises stress) for the torsional process of the CNTB@CNT(3,3) structure.

Different fracture dynamics occurs for CNTBs with larger diameters, as shown in Fig. 3. In this figure we show the MD snapshots for the twisting process of a CNTB formed with CNTs(14,14) at 300 K, from now on referred to as CNTB@CNT(14,14), as the representative case for the systems with larger tube diameters. For the sake of comparison with the case presented above, the morphological deformations of CNTB@CNT(14,14) under torsional loading are also analyzed until its complete fracture. Fig. 3(a)–(e) illustrate the representative MD snapshots for the CNTB@CNT(14,14) subjected to a twisting angle of 0°, 180°, between 272° and 276°, 360°, and 1440°, respectively. It is worthwhile to stress that the video for the MD of CNTB@CNT(14,14) is presented in the ESI.†

The initial stage for the CNTB@CNT(14,14) torsional dynamics is presented in Fig. 3(a). The arrangement of this CTNB species after equilibration also shows small relative displacements between the nanotube-imposed temperature effects. In Fig. 3(b), one can note that each individual CNT of the bundled sample collapses into its centers flattening the tubes structure. From that moment on, the torsional dynamics of CNTB@CNT(14,14) resemble the twisting of interacting nanoribbons. The critical angle for the CNTB@CNT(14,14) is 272°, as shown in Fig. 3(c). Note the angle for the CNTB@CNT(14,14) fracture is substantially smaller than the critical angle for the CNTB@CNT(3,3) failure (about 1005°, as shown in Fig. 2(d)). This result suggests that the larger the tube diameter, the higher the plasticity degree of the bundled sample when subjected to torsional loading.

In Fig. 3(c), the color scheme denotes the ring composition and deformation in the tube structure. This figure was generated using the *PaperChain* representation in VMD.[43] In this procedure, VMD finds all rings up to a user-defined maximum size by scanning the molecular topology. Then, each ring is rendered by fitting a polyhedron to the involved atoms and the ring centroid. In the color scheme adopted for Fig. 3(c), red stands for hexagons. In this way, one can realize that after the critical angle threshold for the CNTB@CNT(14,14) failure (up to 272° of torsion), its fracture occurs near the left edge, which is followed by several hexagon deformations characterized by the blue and purple colors in Fig. 3(c). Further increase in the torsional loading θ = 360° results in the fragmentation of the CNTB@CNT(14,14) as illustrated in Fig. 2(d). The unwrapped nanotubes tend to reassume the tubular form after having one of the edges fractured, while the nanotubes with no crack continue to be collapsed under the torsional stress. At θ = 1440° of twisting angle, as shown in Fig. 3(e), all the nanotubes are fractured and no collapsed region takes place, differently to what was obtained in the CNTB@CNT(3,3) case (see Fig. 2(f)). It is evident that the CNTB@CNT(14,14) has a less distorted profile compared to CNTB@CNT(3,3) in the final stage of the twisting process. This is another piece of evidence that bundle samples composed of nanotubes with large diameters tend to be extremely fragile when upon torsional loading. The ESI† presents a discussion on the shear stress distribution (von-Mises stress) for the torsional process of the CNTB@CNT(14,14) structure.

The accumulated torsional energy (ΔE) as a function of the twisted angle for all the bundled samples studied here is shown in Fig. 4. In this figure, the CNTBs with smaller and larger

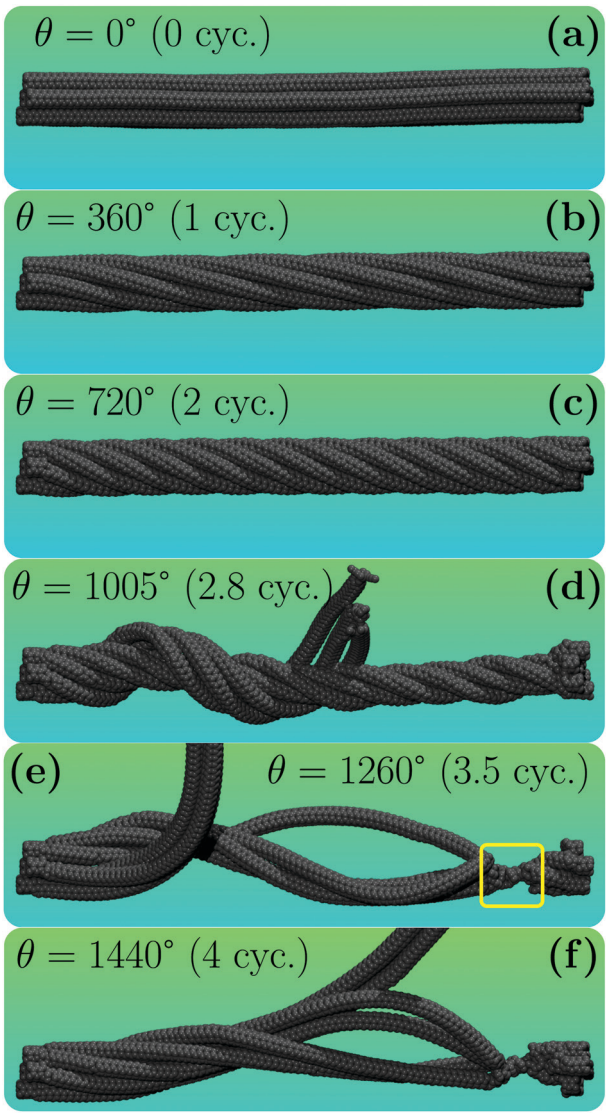

Fig. 2 Representative MD snapshots for the twisting process of a CNTB formed with CNTs(3,3) at 300 K, from now on referred to as CNTB@CNT(3,3). This figure illustrates the MD simulation for the CNTB@CNT(3,3) subjected to a twisting angle or cycle (cyc.) of (a) 0° or 0 cycle, (b) 360° or 1 cycle, (c) 720° or 2 cycles, (d) 1005° or 2.8 cycles, 1260° or 3.5 cycles, and (f) 1440° or 4 cycles.

diameters are presented in different tonalities of green and blue, respectively. ΔE is defined here as the difference between the ground state energy of the CNTB at the beginning of the twisting process and its potential energy at a particular time of the simulation. As a general trend, one can note that ΔE increases continuously until the first point when it drops abruptly. This point represents the CNTB fracture. From the initial slope of the curves, we concluded that the CNTBs exhibit very similar torsion rigidity at the beginning of the loading process regardless of the tube chirality.

As mentioned above, the higher the tube diameter, the higher the plasticity degree of the bundled sample when subjected to torsional loading. In other words, tubes with small diameters are much stiffer. This feature can be noted in Fig. 4, once all the blue lines show their first drop before θ = 360° whereas the green lines drop around θ = 720°. The exception is the dark green curve (CNTB@CNT(3,3)) that has the first drop at approximately θ = 1000°. For all the groups (*i.e.* large and small diameters) one can note that the armchair-based CNTBs—dark blue and dark green lines, which refer to CNTB@CNT(3,3) and CNTB@CNT(14,14), respectively—have higher accumulated energies and, consequently, higher critical angles for the bundle fracture when contrasted with CNTBs composed of zigzag or chiral tubes. One possible reason for this behavior is the almost perfect alignment of the hexagonal rings in the armchair CNTs during their collapse promoted by the torsional loading (*i.e.*, one on top of the other). This alignment, which is not observed in the zigzag and chiral CNTBs, can increase the inter-tube vdW interactions, making the CNTB more stable. Except for the CNTB@CNT(3,3) case, one can note a sequence of small energy drops before the total fracture of the CNTBs, which is represented by the flat pattern in the curves. The CNTB@CNT(3,3) shows only two drops before its fracture. This sequence of energy drops is due to successive structural reconstructions, which are induced by tensions generated during torsional loads that lead to several formations and the breaking of new carbon–carbon bonds. Importantly, this mechanism for the morphological deformation of CNTBs was also observed in deforming, by torsional loading, single carbon and graphyne nanotubes.[47]

In Fig. 5 we present the time evolution for the hybridization percentage as a function of the number of twisting cycles in the CNTB structure during the torsional process. Fig. 5(a)–(f) show the total number of sp^1-like (yellow), sp^2-like (blue), and sp^3-like (red) bonds for the CNTB@CNT(3,3), CNTB@CNT(4,2), CNTB@CNT(5,0), CNTB@CNT(14,14), CNTB@CNT(18,9), and CNTB@CNT(25,0) cases respectively. In Fig. 5, one can observe that the initial CNTBs configuration only presents sp^2-like carbon–carbon bonds, as expected. During the twisting process, the CNTBs composed of tubes with smaller diameters convert a substantial amount of sp^2-like bonds into sp^3-like ones. Between 30–50% of bonds were converted, as depicted in Fig. 5(a–c). This conversion process takes place until the bundles fracture. After the critical twisting cycles (*i.e.*, after the bundles fracture) one can note in Fig. 5(a–c) the coexistence of sp^2-like and sp^3-like bond types. These two bond types remained until the end of the simulation, but with a predominance of sp^2-like bonds, indicating the presence of structural deformations, as illustrated in the yellow square in Fig. 2(e). On the other hand, in Fig. 5(d–f), one can note that a substantially smaller percentage of sp^2-like bonds is converted to sp^3-like ones during the twisting process (about 25%), in contrast with the cases shown in Fig. 59(a–c). This trend indicates that CNTBs composed of tubes with large diameters are less susceptible to morphological deformations. Moreover, the percentage of sp^2-like bonds is restored to its initial value at the end of the simulation, as depicted in Fig. 5(d–f). In all the cases, the percentage of sp^1-like bonds was not altered, remaining always at zero.

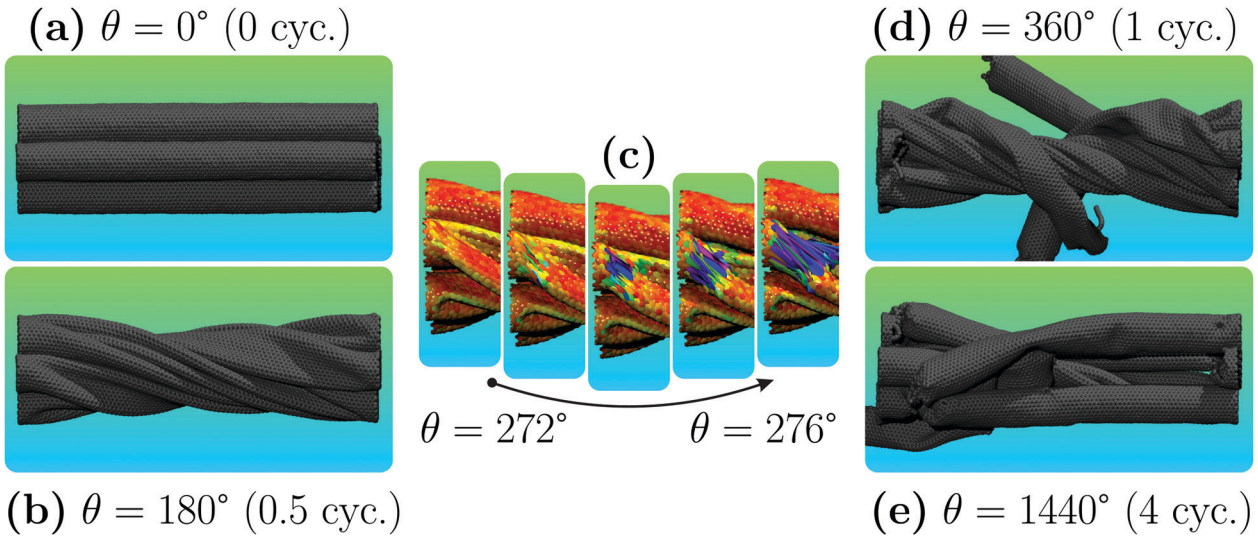

Fig. 3 Representative MD snapshots for the twisting process of a CNTB formed with CNTs(14,14) at 300 K, from now on referred to as CNTB@CNT(14,14). This figure illustrates the MD simulation for the CNTB@CNT(14,14) subjected to a twisting angle or cycle (cyc.) of (a) 0° or 0 cycle, (b) 180° or 0.5 cycle, (c) between 272° and 276°, (d) 360° or 1 cycle, and (e) 1440° or 4 cycles. The color scheme in panel (c) denotes the ring composition and deformation in the tube structure, where red stands for hexagons.

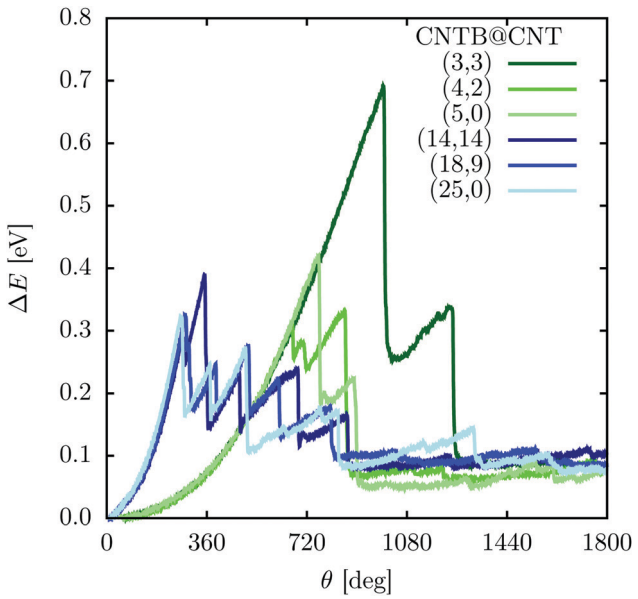

Fig. 4 Accumulated torsional energy (ΔE) as a function of the twisted angle for all the bundled samples. CNTBs with smaller and larger diameters are presented in different tonalities of green and blue, respectively.

One striking result is the formation of a diamondoid-like region in the twisting process of CNTBs with a small diameter. For the sake of clarity, we placed in the top panel of Fig. 6 the MD snapshot presented in Fig. 2(e). The bottom panel of this figure enlarges the yellow square highlighted in the top panel, and the yellow bonds denote the diamondoid-like core. The shape of this diamondoid structure is similar to other diamondoid cores reported in the literature.[21,22] This morphological transformation reveals a relevant result once it suggests a new synthesis route for converting nanotubes into diamonds.

4 Summary and conclusions

In summary, we carried out fully atomistic reactive MD simulations to investigate the torsional fracture of CNTBs. We considered CNTBs of different diameters and chiralities. Our findings show that the CNTB fracture patterns are diameter-dependent. One can conclude that the CNTB fracture processes occur in the same fashion for tubes with a similar diameter. Moreover, our results suggest that the larger the tube diameter, the higher the plasticity degree of the bundled sample when subjected to torsional loading. By using MD snapshots, we were able to describe in detail the fracture process of CNTBs, and the products yielded after their failure.

We analyzed the time evolution of accumulated torsional energy (ΔE). This quantity revealed crucial details of the fracture process of CNTBs. Generally, ΔE increases continuously until the first point when it drops abruptly. This point represents the CNTB fracture. From the initial slope of the curves, one can conclude that the CNTBs exhibit very similar torsion rigidity at the beginning of the loading process regardless of the tube chirality. The armchair-based CNTBs presented higher accumulated energies and, consequently, higher critical angles for the bundle fracture when contrasted with CNTBs composed of zigzag or chiral tubes. A reason that explains this behavior is the almost perfect alignment of the hexagonal rings in the armchair CNTs during their collapse promoted by the torsional loading (*i.e.*, one on top of the other). This alignment, which is not observed in the zigzag and chiral CNTBs, can increase the inter-tube vdW interactions, making the CNTB more stable.

The time evolution for the hybridization percentage as a function of the number of twisting cycles in the CNTB structure during the torsional process was also discussed. The initial CNTB configuration only presents sp^2-like carbon–carbon bonds, as expected. During the twisting process, the sp^2-like

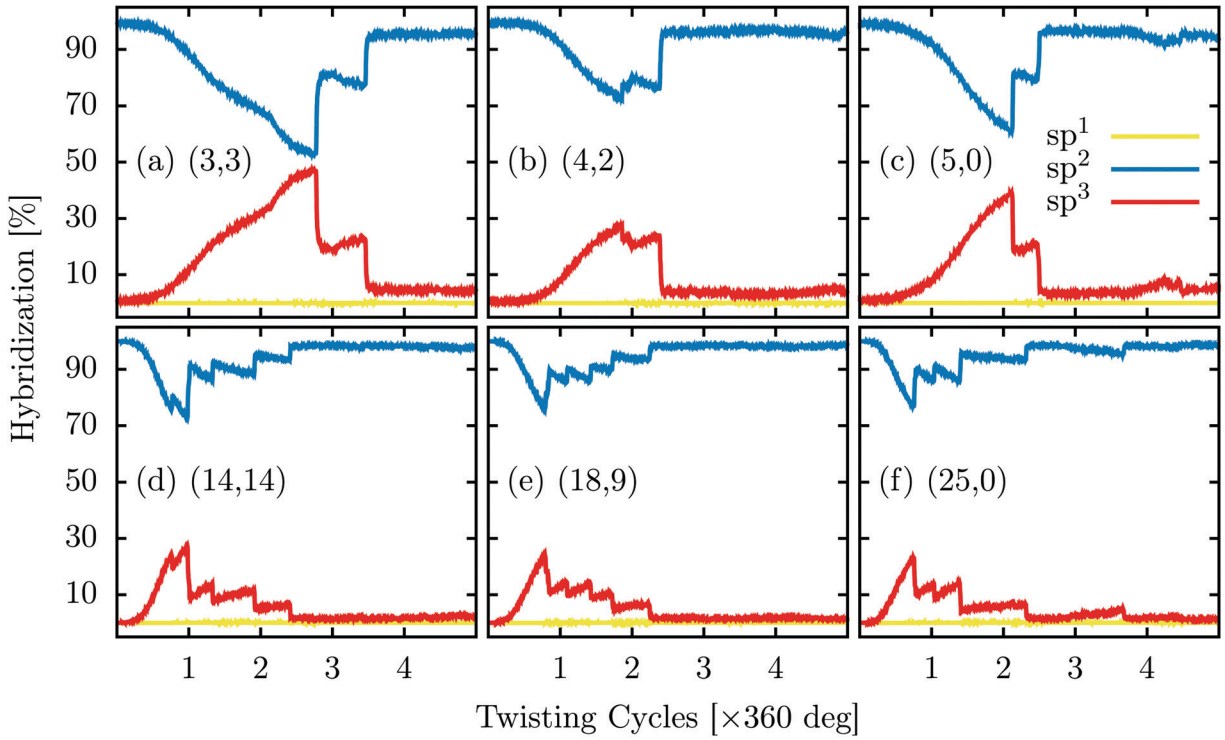

Fig. 5 Time evolution for the hybridization percentage as a function of the number of twisting cycles in the CNTB structure during the torsional process.

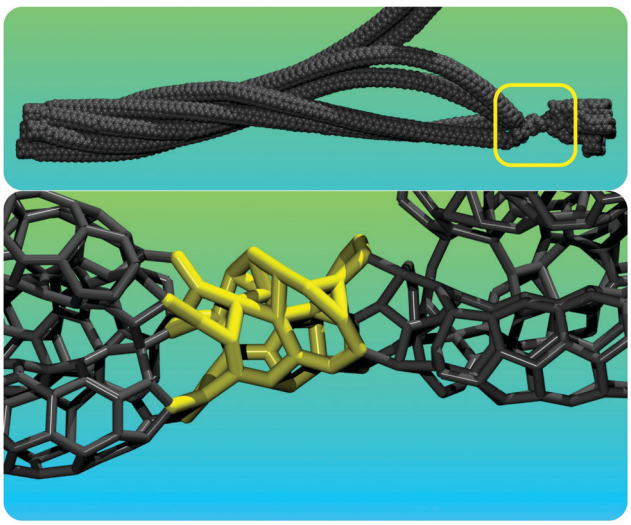

Fig. 6 Diamondoid-like core formation in the torsional process of CNTB@CNT(3,3). The bottom panel of this figure enlarges the yellow square highlighted in the top panel, and the yellow bonds denote the diamondoid-like core.

bonds are converted into sp^3-like ones. This conversion process takes place until the bundles fracture. After the critical twisting cycles, one can note the coexistence of sp^2-like and sp^3-like bond types for the CNTB species with small diameters. Remarkably, this coexistence of bond types revealed the formation of a diamondoid-like region in the twisting process of CNTBs with a small diameter. This morphological transformation points to a relevant result once it suggests a new synthesis route for converting nanotubes into diamonds.

Conflicts of interest

There are no conflicts to declare.

Acknowledgements

The authors gratefully acknowledge the financial support from Brazilian research agencies CNPq, FAPESP, and FAP-DF. L. A. R. J. acknowledges the financial support from a Brazilian Research Council FAP-DF grants 00193 – 00000853/2021 – 28 and 00193 – 00000811/2021 – 97 and CNPq grant 302236/2018 – 0, respectively. W. F. C acknowledges the financial support from FAPDF grant 00193 – 00000857/2021 – 14. L. A. R. J. thanks CENAPAD-SP for providing the computational facilities. L. A. R. J. gratefully acknowledges the financial support from IFD/UnB (Edital 01/2020) grant 23106.090790/2020 – 86. L. A. R. J. gratefully acknowledges the support from ABIN grant 08/2019. The authors thank the National Laboratory for Scientific Computing (LNCC/MCTI, Brazil) for providing HPC resources of the SDumont supercomputer, which have contributed to the research results reported within this paper. URL: http://sdumont.lncc.br. M. L. P. J. and L. A. R. J. acknowledge Núcleo de Computação de Alto Desempenho (NACAD) for providing the computational facilities through the Lobo Carneiro supercomputer. L. A. R. J. thanks Fundação de Apoio à

Pesquisa (FUNAPE), Edital 02/2002 - Formulário de Inscrição N.4, for the financial support.

References

1 S. Iijima and T. Ichihashi, *Nature*, 1993, **363**, 603–605.
2 S. Iijima, P. Ajayan and T. Ichihashi, *Phys. Rev. Lett.*, 1992, **69**, 3100.
3 S. Iijima, C. Brabec, A. Maiti and J. Bernholc, *J. Chem. Phys.*, 1996, **104**, 2089–2092.
4 F. Wen, F. Zhang and Z. Liu, *J. Phys. Chem. C*, 2011, **115**, 14025–14030.
5 D. S. Hecht, L. Hu and G. Irvin, *Adv. Mater.*, 2011, **23**, 1482–1513.
6 R. S. Ruoff and D. C. Lorents, *Carbon*, 1995, **33**, 925–930.
7 T. Ebbesen, H. Lezec, H. Hiura, J. Bennett, H. Ghaemi and T. Thio, *Nature*, 1996, **382**, 54–56.
8 P. S. Prabha, I. Ragavi, R. Rajesh and M. P. Kumar, *Mater. Today: Proc.*, 2021, **46**, 3937–3940.
9 K. Mylvaganam and L. Zhang, *Nanotechnology*, 2007, **18**, 475701.
10 A. K. Huttel, G. A. Steele, B. Witkamp, M. Poot, L. P. Kouwenhoven and H. S. van der Zant, *Nano Lett.*, 2009, **9**, 2547–2552.
11 S. Legoas, V. Coluci, S. Braga, P. Coura, S. Dantas and D. S. Galvao, *Phys. Rev. Lett.*, 2003, **90**, 055504.
12 I. V. Zaporotskova, N. P. Boroznina, Y. N. Parkhomenko and L. V. Kozhitov, *Modern Electron. Mater.*, 2016, **2**, 95–105.
13 Q. Zhao, Z. Gan and Q. Zhuang, *Electroanalysis*, 2002, **14**, 1609–1613.
14 A. Dillon, *Chem. Rev.*, 2010, **110**, 6856–6872.
15 L. Wen, F. Li and H.-M. Cheng, *Adv. Mater.*, 2016, **28**, 4306–4337.
16 S. Heinze, J. Tersoff, R. Martel, V. Derycke, J. Appenzeller and P. Avouris, *Phys. Rev. Lett.*, 2002, **89**, 106801.
17 P. Jarillo-Herrero, J. A. Van Dam and L. P. Kouwenhoven, *Nature*, 2006, **439**, 953–956.
18 K. Liew, C. Wong and M. Tan, *Appl. Phys. Lett.*, 2005, **87**, 041901.
19 S. Iijima, *Phys. B: Condens. Matter*, 2002, **323**, 1–5.
20 Y. Bai, R. Zhang, X. Ye, Z. Zhu, H. Xie, B. Shen, D. Cai, B. Liu, C. Zhang and Z. Jia, *et al.*, *Nat. Nanotechnol.*, 2018, **13**, 589–595.
21 K.-W. Yeung, Y. Dong, L. Chen, C.-Y. Tang, W.-C. Law and G. C.-P. Tsui, *Nanotechnol. Rev.*, 2020, **9**, 650–669.
22 S. Park, I. I. Abate, J. Liu, C. Wang, J. E. Dahl, R. M. Carlson, L. Yang, V. B. Prakapenka, E. Greenberg and T. P. Devereaux, *et al.*, *Sci. Adv.*, 2020, **6**, eaay9405.
23 M. D. Lima, N. Li, M. Jung de Andrade, S. Fang, J. Oh, G. M. Spinks, M. E. Kozlov, C. S. Haines, D. Suh and J. Foroughi, *et al.*, *Science*, 2012, **338**, 928–932.
24 Y. Bai, H. Yue, R. Zhang, W. Qian, Z. Zhang and F. Wei, *Acc. Mater. Res.*, 2021, **2**, 998–1009.
25 M. Peters, L. E. Mcneil, J. P. Lu and D. Kahn, *Phys. Rev. B: Condens. Matter Mater. Phys.*, 2000, **61**, 5939.
26 J. Foroughi, G. M. Spinks, G. G. Wallace, J. Oh, M. E. Kozlov, S. Fang, T. Mirfakhrai, J. D. Madden, M. K. Shin and S. J. Kim, *et al.*, *Science*, 2011, **334**, 494–497.
27 Z.-L. Zhao, H.-P. Zhao, J.-S. Wang, Z. Zhang and X.-Q. Feng, *J. Mech. Phys. Solids*, 2014, **71**, 64–83.
28 P. Wang, H. Zhan and Y. Gu, *ACS Appl. Nano Mater.*, 2020, **3**, 10218–10225.
29 B.-W. Jeong, *J. Nanomater.*, 2012, **2012**, 1–6.
30 D. Asadollahi and M. Shariati, *Acta Mech.*, 2021, **232**, 2425–2441.
31 A. L. Zadeh, M. Shariati and H. Torabi, *J. Phys. Chem. Solids*, 2012, **73**, 1282–1289.
32 Y.-K. Kwon and D. Tománek, *Phys. Rev. Lett.*, 2000, **84**, 1483.
33 K. Liew, C. Wong and M. Tan, *J. Appl. Phys.*, 2006, **99**, 114312.
34 R. Mirzaeifar, Z. Qin and M. J. Buehler, *Nanoscale*, 2015, **7**, 5435–5445.
35 H. Wei, H. Z. J. Ting, Y. Gong, C. Lü, O. E. Glukhova and H. Zhan, *Nanomaterials*, 2022, **12**, 760.
36 H. Zhan, G. Zhang, J. M. Bell, V. B. Tan and Y. Gu, *Nat. Commun.*, 2020, **11**, 1–11.
37 J. Wallace, D. Chen and L. Shao, *J. Appl. Phys.*, 2020, **128**, 195902.
38 Z. Zhang, B. Liu, Y.-W. Zhang, K.-C. Hwang and H. Gao, *Carbon*, 2014, **77**, 1040–1053.
39 S. Plimpton, *J. Comput. Phys.*, 1995, **117**, 1–19.
40 S. J. Stuart, A. B. Tutein and J. A. Harrison, *J. Chem. Phys.*, 2000, **112**, 6472–6486.
41 L.-C. Qin, *Phys. Chem. Chem. Phys.*, 2007, **9**, 31–48.
42 S. Melchor and J. A. Dobado, *J. Chem. Inf. Comput. Sci.*, 2004, **44**, 1639–1646.
43 W. Humphrey, A. Dalke and K. Schulten, *et al.*, *J. Mol. Graphics*, 1996, **14**, 33–38.
44 L. Verlet, *Phys. Rev.*, 1967, **159**, 98.
45 H. C. Andersen, *J. Chem. Phys.*, 1980, **72**, 2384–2393.
46 W. G. Hoover, *Phys. Rev. A: At., Mol., Opt. Phys.*, 1985, **31**, 1695.
47 J. M. de Sousa, G. Brunetto, V. R. Coluci and D. S. Galvao, *Carbon*, 2016, **96**, 14–19.

